

# Active Simultaneously Transmitting and Reflecting Surface Assisted NOMA Networks

Xinwei Yue, *Senior Member, IEEE*, Jin Xie, Chongjun Ouyang, Yuanwei Liu, *Senior Member, IEEE*, Xia Shen and Zhiguo Ding, *Fellow, IEEE*

## Abstract

The novel active simultaneously transmitting and reflecting surface (ASTARS) has recently received a lot of attention due to its capability to conquer the multiplicative fading loss and achieve full-space smart radio environments. This paper introduces the ASTARS to assist non-orthogonal multiple access (NOMA) communications, where the stochastic geometry theory is used to model the spatial positions of pairing users. We design the independent reflection/transmission phase-shift controllers of ASTARS to align the phases of cascaded channels at pairing users. We derive new closed-form and asymptotic expressions of the outage probability and ergodic data rate for ASTARS-NOMA networks in the presence of perfect/imperfect successive interference cancellation (pSIC). The diversity orders and multiplexing gains for ASTARS-NOMA are derived to provide more insights. Furthermore, the system throughputs of ASTARS-NOMA are investigated in both delay-tolerant and delay-limited transmission modes. The numerical results are presented and show that: 1) ASTARS-NOMA with pSIC outperforms ASTARS assisted-orthogonal multiple access (ASTARS-OMA) in terms of outage probability and ergodic data rate; 2) The outage probability of ASTARS-NOMA can be further reduced within a certain range by

X. Yue and J. Xie are with the Key Laboratory of Information and Communication Systems, Ministry of Information Industry and also with the Key Laboratory of Modern Measurement & Control Technology, Ministry of Education, Beijing Information Science and Technology University, Beijing 100101, China (email: {xinwei.yue and jin.xie}@bistu.edu.cn).

Chongjun Ouyang is with the School of Information and Communication Engineering, Beijing University of Posts and Telecommunications, Beijing, 100876, China (e-mail: dragonaim@bupt.edu.cn).

Y. Liu is with the School of Electronic Engineering and Computer Science, Queen Mary University of London, London E1 4NS, U.K. (email: yuanwei.liu@qmul.ac.uk).

X. Shen is with the China Academy of Information and Communications Technology (CAICT), Beijing 100191, China (email: shenxia@caict.ac.cn).

Z. Ding is with the Department of Electrical Engineering And Computer Science, Khalifa University, Abu Dhabi, UAE, and also with Department of Electrical Engineering, Princeton University, Princeton, USA (e-mail: zhiguo.ding@gmail.com).

increasing the power amplification factors; 3) The system throughputs of ASTARS-NOMA are superior to that of ASTARS-OMA in both delay-limited and delay-tolerant transmission modes.

***Index terms***— Active simultaneously transmitting and reflecting surface, non-orthogonal multiple access, stochastic geometry.

## I. INTRODUCTION

As the number of device in wireless networks explosively grows, the sixth-generation (6G) wireless networks are facing unprecedented challenges for providing high-speed, low-latency data services for massive users [1, 2]. From the standpoint of expanding capacity, signal strength, and coverage range, the reconfigurable intelligent surface (RIS) boasts remarkable capabilities. It has been considered as one of promising technologies of 6G networks [3]. Essentially, passive RIS (PRIS) is a planar surface comprising abundant inexpensive passive reflecting components, which is able to modify the phase and amplitude of incident signals to achieve smart radio environments [4]. In addition, PRIS has been shown to be able to improve the performance of physical layer security [5], user localization [6] and unmanned aerial vehicle communications [7].

Despite of the aforementioned advantages of PRIS, it only provides the half-space smart transmissions [8, 9]. The innovative simultaneously transmitting and reflecting surfaces (STARS), which can achieve full spatial coverage, was proposed to get around this restriction [10]. Specifically, a passive STARS (PSTARS) integrates many passive simultaneously transmitting and reflecting elements that can transmit and reflect the incident signals [11]. Based on hardware architecture and physical principles, the authors in [12] further studied mode switching, energy splitting and time switching protocols for PSTARS networks. For these three protocols, the authors of [13] investigated the minimization of power consumption in PSTARS networks. The impact of separate codebooks on PSTARS was examined in terms of detection capabilities and system performance without complete channel state information (CSI) [14]. To enhance channel conditions, the authors in [15] incorporated PSTARS into the over-the-air computation system, enabling excellent learning accuracy and privacy perservation over large coverage areas. In [16], the authors employed a diversity-preserving phase-shift strategy to attain complete diversity order of PSTARS networks by taking into account coupled phase-shift models. As a further development, the authors in [17] evaluated the secrecy capacity of PSTARS networks with coupled phase-shift scheme.

Widespread interests have also been drawn to non-orthogonal multiple access (NOMA) which is a potential multiple access method for the next generation of wireless communication networks [18, 19]. NOMA has the ability to boost system throughput, capacity and energy efficiency in comparison to orthogonal multiple access (OMA), delivering an improved communication service for large numbers of users [20]. The notion of cooperative NOMA was introduced in [21], where one cell-centred user is utilized as a relay to enhance the quality of service for an edge user. Inspired by this work, the ergodic data rate and outage probability of full/half-duplex cooperative NOMA networks were studied in [22]. The authors integrated PRIS into NOMA networks [23], where the effect of stochastic discrete and coherent phase-shifting designs was researched for PRIS-NOMA networks. With the focus on green communications, the authors of [24] revealed the tradeoff between maximizing the sum rate and minimizing the power budget in PRIS-assisted NOMA networks. Considering complexity expansion and error propagation issues, the authors in [25] studied the ergodic data rate and outage performances of PRIS-NOMA with perfect/imperfect successive interference cancellation (pSIC/ipSIC) schemes. Recently, a new concept of near-field NOMA communication was introduced in [26], which benefits from the beamforming characteristics of near-field to enable NOMA in both angular and distance domains. Moreover, the authors of [27] utilized pre-configured spatial beams to serve both near-field and far-field users, confirming that NOMA can effectively support the coexistence of near-field and far-field communications.

As mentioned above, the integration of NOMA with other technologies is flourishing, and the PSTARS-assisted NOMA (PSTARS-NOMA) networks naturally becomes a promising direction. The superiority of NOMA related on the differentiated channel conditions among users [28], and thus the establishment of channel condition differences was essential for NOMA. With the help of PSTARS, the users can be deployed to different half-spaces with vastly disparate channel conditions, thereby augmenting the performance of NOMA [29]. From the perspective of performance analysis, the outage performance of PSTARS-NOMA was evaluated by utilizing the central limit theorem and curve fitting model [30]. On the basis of these models, the authors of [31] analyzed the ergodic data rate, outage behaviors and system throughput of PSTARS-NOMA with pSIC/ipSIC schemes. The coverage characteristics of PSTARS networks were surveyed in [32], where the coverage of PSTARS-NOMA can be significantly extended compared to PSTARS-OMA. In the presence of Nakagami- $m$  cascade channels, the secrecy outage probability of PSTARS-NOMA was researched in [33] by considering the residual hardware impairments.

The authors of [34] researched a matching theory based channels allocation scheme to achieve the maximum sum rate of PSATRS-NOMA systems. In [35], over-the-air federated learning and PSTARS-NOMA were integrated into an unified framework, which achieves both high spectral efficiency and learning performance.

While PRIS/PSTARS bring the enhanced performance of wireless networks, they also cause multiplicative fading loss. Specifically, the small-scale fading of transmitter-PSTARS/PRIS link and PSTARS/PRIS-receiver link were multiplied, which is usually worse than direct-link fading [36]. To eliminate this effect, an active RIS (ARIS) with integrated reflection-type amplifiers has been proposed [37], which magnifies the signals' power, and then reflect to the desired users. The simulation results demonstrated that the service area coverage and spectral efficiency of ARIS were superior to those of PRIS [38]. Condition on the same power consumption, the authors of [39] revealed that ARIS outperforms PRIS in terms of the achievable data rate if the number of elements is small. In energy-constrained internet-of-things systems, ARIS-NOMA was proven to achieve higher system throughput than ARIS-OMA [40]. A subarray-based ARIS structure was designed to improve energy efficiency [41], where each subarray can be independently controlled. Recently, a novel hardware model for active STARS (ASTARS) was proposed [42], which has the ability to offset the multiplicative fading loss and achieve full-space coverage. In [43], the authors confirmed that ASTARS-aided communication systems outperform ARIS in terms of the sum-rate improvement and power consumption reduction. Moreover, the maximum secrecy rate of ASTARS assisted wireless networks was achieved by jointly optimizing the configuration of elements and beamforming of access points [44].

#### *A. Motivation and Contributions*

As a new topic, only a few works have been researched for ASTARS networks, where the hardware model design [42], sum rate maximisation [43] and system security [44] have been the focus of the previous works. Since ASTARS is able to provide different channel differences and amplify the desired signals for non-orthogonal users, the physical layer performance analysis of ASTARS assisted NOMA networks is necessary to gain valuable insights. To the best of our knowledge, the integration of ASTARS with NOMA networks have not been researched yet, and the critical questions require further exploration. In particularly, considering the issues of complexity scaling and error propagation, it is important to analyse the effect of ipSIC on ASTARS-NOMA networks. The impact of the ASTARS elements' configuration affects on the

performance of ASTARS-NOMA networks is still unknown. Inspired by these motivations, we introduce an ASTARS to assist NOMA communications by invoking stochastic geometry, where the pairing users, i.e.,  $U_r$  and  $U_t$  are randomly distributed within contralateral area of ASTARS. More particularly, we evaluate the outage probability, system throughput, and ergodic data rate for  $U_r$  with pSIC/ipSIC and  $U_t$ . In summary, the following are the primary contributions of this paper:

- 1) We propose ASTARS-NOMA networks with randomly deployed pairing users, where  $U_r$  and  $U_t$  are located at the opposite sides of ASTARS for NOMA transmission. We design the independent reflection/transmission phase-shift controllers of ASTARS to align the phases of the cascaded channels at  $U_r$  and  $U_t$ , respectively. We derive the closed-form expressions of the outage probability for  $U_r$  with pSIC/ipSIC and  $U_t$  by invoking the stochastic geometry. We also investigate the system throughput of ASTARS-NOMA in the delay-limited transmission mode.
- 2) We derive the asymptotic expressions of the outage probability for  $U_r$  with pSIC/ipSIC and  $U_t$  by utilising Laplace transforms and convolution theorem. The diversity orders of  $U_r$  with pSIC/ipSIC and  $U_t$  in the high SNR region are calculated, respectively. We confirm that the diversity orders of  $U_r$  with pSIC and  $U_t$  are proportional to the quantities of ASTARS elements. The outage probability of  $U_r$  with ipSIC converges to an error floor due to the residual interference, and the corresponding diversity order is equal to *zero*.
- 3) We derive the closed-form expressions of ergodic data rate for  $U_r$  with pSIC/ipSIC and  $U_t$ . We further derive asymptotic expressions of ergodic data rate for  $U_r$  with ipSIC and  $U_t$  within high SNR region. Based on Jensen's inequality, we provide an upper bound on  $U_r$ 's ergodic data rate with pSIC. On the basis of approximated analyses, we survey the multiplexing gains for  $U_r$  and  $U_t$ . Moreover, the system throughputs of ASTARS-NOMA are evaluated in the delay-tolerant transmission mode.
- 4) We compare the performance of ASTARS-NOMA with ASTARS-OMA and PSTARS-NOMA in terms of the outage probability, system throughput, and ergodic data rate. We reveal that both the outage probability and ergodic data rate of ASTARS-NOMA with pSIC performs better than ASTARS-OMA. On the condition of equipping with less ASTARS elements, ASTARS-NOMA is capable of furnishing the enhanced performance relative to PSTARS-NOMA. We further demonstrate that the outage behaviors of ASTARS-NOMA

can be further improved within a certain range by increasing the power amplification factors.

### B. Organization and Notations

The rest of this article is divided into the following sections. Section II presents the system model of ASTARS-NOMA in terms of hardware architecture, network deployment, and channel statistics. The outage probability expressions of ASTARS-NOMA are derived in Section III, in which the diversity orders for  $U_r$  and  $U_t$  are provided. Section IV evaluates the ergodic data rate of  $U_r$  and  $U_t$ . The simulation results and the corresponding analyses are presented in Section V. Then the conclusions of this paper are given in Section VI, and Appendix contains a collection of mathematical proofs.

The main symbols used in this article are as follows: The probability density function (PDF) of a random variable  $X$  is denoted as  $f_X(\cdot)$ , and its cumulative distribution function (CDF) is denoted as  $F_X(\cdot)$ .  $\mathbb{E}\{\cdot\}$  denotes the expectation and  $\mathbb{D}\{\cdot\}$  denotes variance operations;  $(\cdot)^H$  stands for conjugate-transpose operation.

## II. SYSTEM-MODEL

We consider an ASTARS-aided downlink NOMA communication scenario as illustrated in Fig. 1(a), in which the incident signals from the base station (BS) are amplified and reflected or refracted to the users. The pairing users and BS are both equipped with a single antenna, while the ASTARS is made up of  $L$  ASTARS elements. Assume that the users are stochastically distributed in a circular region  $\mathbb{O}_D$  with radius  $D$ , and ASTARS is fixed in the center of  $\mathbb{O}_D$ . More precisely, this circular region is separated by ASTARS into two parts denoted by the reflection region and transmission region, respectively. Two users are randomly selected from the reflection and transmission regions, and are denoted by  $U_r$  and  $U_t$ , respectively. Due to the influence of obstacle blockage, assuming that the direct link from BS to  $U_r$  and  $U_t$  are not available or even in a state of complete outage. From the perspective of hardware design shown in Fig. 2, the element of ASTARS integrates active amplifiers for enlarging the incident signals to overcome the attenuation effect of multiplicative fading. Such integrated amplifiers can be implemented with many existing active devices, such as integrated chips [45], the asymmetric current mirror [46] or the current-inverting converter [47], which can significantly improve energy and hardware efficiency. Power splitting can be achieved by the harmonic components of power system [48].

The complex channel coefficients from the BS to ASTARS, and then from ASTARS to  $U_\varphi$  are denoted by  $\mathbf{h}_s \in \mathbb{C}^{L \times 1}$  and  $\mathbf{h}_\varphi \in \mathbb{C}^{L \times 1}$  with  $\varphi \in \{r, t\}$ , respectively. For practical considerations, the ASTARS-NOMA networks' wireless communication links undergo Rician fading.  $\mathbf{h}_r^H \Theta_r \mathbf{h}_s$  and  $\mathbf{h}_t^H \Theta_t \mathbf{h}_s$  separately stand for the cascade complex channel coefficients from the BS to ASTARS, and then to  $U_r$  and  $U_t$ , where  $\Theta_r = \sqrt{\lambda \beta_r} \text{diag}(e^{j\theta_1^r}, \dots, e^{j\theta_L^r}, \dots, e^{j\theta_L^r}) = \sqrt{\lambda \beta_r} \Phi_r$  and  $\Theta_t = \sqrt{\lambda \beta_t} \text{diag}(e^{j\theta_1^t}, \dots, e^{j\theta_L^t}, \dots, e^{j\theta_L^t}) = \sqrt{\lambda \beta_t} \Phi_t$  denote the reflection and transmission phase-shifting amplification matrixes of ASTARS, respectively. To facilitate analysis, assume that all ASTARS elements have the same amplification factor  $\lambda$  and  $\lambda > 1$ .  $\beta_r$  and  $\beta_t$  are denoted by the reflection and transmission amplitude coefficients, where  $\beta_r + \beta_t \leq 1$ .  $\theta_l^r, \theta_l^t \in [0, 2\pi)$  represent the transmission and reflection response's phase-shift of the  $l$ -th element, respectively. Since the transmission and reflection phase shifts are controlled by two different phase-shifters,  $\theta_l^r$  and  $\theta_l^t$  can be tuned independently. The perfect CSI is required for the users to carry out coherent demodulation.

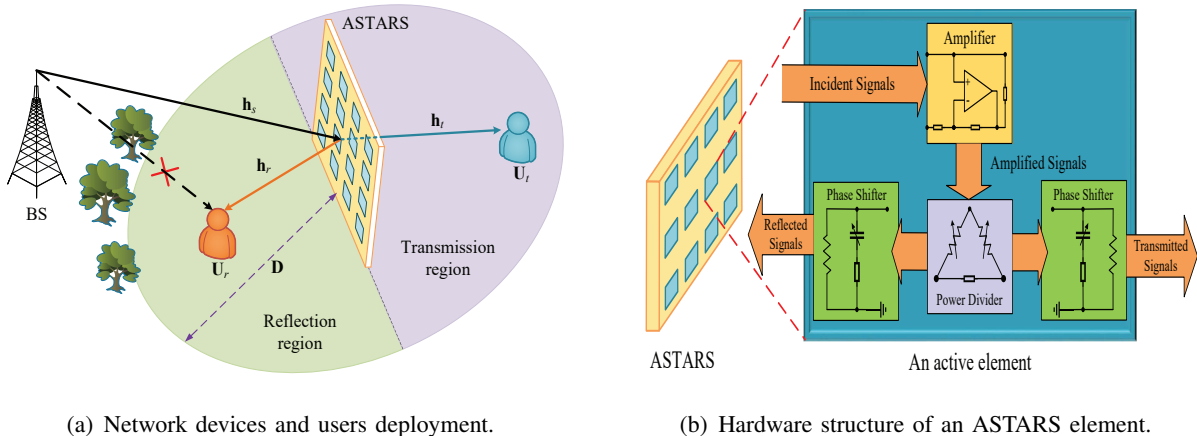


Fig. 1: System model of ASTARS-NOMA networks.

### A. Signal Model of Pairing Users

In ASTARS-NOMA networks, channels differences between users can be created by adjusting the energy coefficients of reflection and transmission [30]. In this paper, we assign more energy coefficient to the users in reflection area, resulting in  $U_r$  being the strong user and  $U_t$  being the weak user. Based on the principle of NOMA,  $U_r$  carries out the SIC process. To be specific,  $U_r$  and  $U_t$  receive the amplified superimposed signals reflected/transmitted from ASTARS and

thermal noise generated by active components. At this moment, the received signal expressions at  $U_r$  and  $U_t$  can be separately written as

$$y_r = \mathbf{h}_r^H \Theta_r \mathbf{h}_s \sqrt{P_s^{act}} X_\Sigma + \mathbf{h}_r^H \Theta_r \mathbf{n}_s + \tilde{n}_r, \quad (1)$$

and

$$y_t = \mathbf{h}_t^H \Theta_t \mathbf{h}_s \sqrt{P_s^{act}} X_\Sigma + \mathbf{h}_t^H \Theta_t \mathbf{n}_s + \tilde{n}_t, \quad (2)$$

where  $X_\Sigma = \sqrt{a_r} x_r + \sqrt{a_t} x_t$ ,  $P_s^{act}$  denote BS's transmit power,  $x_r$  and  $x_t$  denote the signals of  $U_r$  and  $U_t$ , respectively.  $a_r$  and  $a_t$  stands for the power allocation factor of  $U_r$  and  $U_t$ , respectively. For the sake of fairness,  $a_r$  and  $a_t$  satisfy the relation  $a_r \leq a_t$  and  $a_r + a_t = 1$ .  $\mathbf{n}_s = [n_s^1, \dots, n_s^l, \dots, n_s^L]^H$  is denoted by the thermal noise matrix generated by ASTARS elements and  $n_s^l \sim \mathcal{CN}(0, \sigma_s^2)$ .  $\tilde{n}_\varphi \sim \mathcal{CN}(0, \sigma_0^2)$  stands for white Gaussian noise with average power  $\sigma_0^2$ . Let  $\mathbf{h}_s = \sqrt{\eta_0 d_s^{-\alpha}} [h_s^1, \dots, h_s^l, \dots, h_s^L]^H$ ,  $\mathbf{h}_\varphi = \sqrt{\eta_0 d_\varphi^{-\alpha}} [h_\varphi^1, \dots, h_\varphi^l, \dots, h_\varphi^L]^H$  denote the channel coefficients from the BS to ASTARS, and then from ASTARS to  $U_\varphi$ , where  $h_s^l = \sqrt{\frac{\kappa}{\kappa+1}} + \sqrt{\frac{1}{\kappa+1}} \tilde{h}_s^l$ ,  $\tilde{h}_s^l \sim \mathcal{CN}(0, 1)$ ,  $h_\varphi^l = \sqrt{\frac{\kappa}{\kappa+1}} + \sqrt{\frac{1}{\kappa+1}} \tilde{h}_\varphi^l$ ,  $\tilde{h}_\varphi^l \sim \mathcal{CN}(0, 1)$ ,  $\kappa$  denotes the Rician factor and  $\alpha$  is path loss exponent,  $\eta_0$  expresses the path loss,  $d_s$  stands for the distances from BS to ASTARS, and  $d_\varphi$  stand for the distance from ASTARS to  $U_\varphi$ .  $U_r$  has better channel conditions and carried out the SIC to firstly detect the signal  $x_t$  of  $U_t$ . Hence, the signal-plus-interference-to-noise ratio (SINR) for  $U_r$  to decode  $x_t$  can be expressed as

$$\gamma_{r \rightarrow t} = \frac{a_t \lambda \beta_r P_s^{act} |\mathbf{h}_r^H \Phi_r \mathbf{h}_s|^2}{a_r \lambda \beta_r P_s^{act} |\mathbf{h}_r^H \Phi_r \mathbf{h}_s|^2 + \lambda \beta_r |\mathbf{h}_r^H \Phi_r \mathbf{n}_s|^2 + \sigma_0^2}. \quad (3)$$

After decoding and deleting  $x_t$ , the SNR for  $U_r$  to decode its own information can be expressed as

$$\gamma_r = \frac{a_r \lambda \beta_r P_s^{act} |\mathbf{h}_r^H \Phi_r \mathbf{h}_s|^2}{\lambda \beta_r |\mathbf{h}_r^H \Phi_r \mathbf{n}_s|^2 + \varepsilon |h_{re}|^2 P_s^{act} + \sigma_0^2}, \quad (4)$$

where  $h_{re} \sim \mathcal{CN}(0, \sigma_{re}^2)$  stands for the residual interference caused by ipSIC. In particular,  $\varepsilon = 0$  stands for pSIC and  $\varepsilon = 1$  denotes ipSIC, respectively.

$U_t$  has weak channel conditions and thus regard  $x_t$  and thermal noise as interference. The SINR for detecting  $x_t$  can be given by

$$\gamma_t = \frac{a_t \lambda \beta_t P_s^{act} |\mathbf{h}_t^H \Phi_t \mathbf{h}_s|^2}{a_r \lambda \beta_t P_s^{act} |\mathbf{h}_t^H \Phi_t \mathbf{h}_s|^2 + \lambda \beta_t |\mathbf{h}_t^H \Phi_t \mathbf{n}_s|^2 + \sigma_0^2}. \quad (5)$$

## B. Statistics Property of Channels

The statistical characteristics of cascade Rician channels employed in ASTARS-NOMA networks are first provided in this subsection, and the spatial impacts on  $U_r$  and  $U_t$  are then evaluated.

1) *Cascade rician distribution*: As ASTARS can independently control reflection and transmission phase-shifts, we configure  $\theta_l^r$  and  $\theta_l^t$  to align the cascaded channels' phase at  $U_r$  and  $U_t$ , respectively. Thus the cascade Rician channels gain  $|\mathbf{h}_\varphi^H \Phi_\varphi \mathbf{h}_s|^2$  can be rewritten as  $\eta_0^2 (d_s d_\varphi)^{-\alpha} \left| \sum_{l=1}^L |h_s^l h_\varphi^l| \right|^2$ . Let  $X_\varphi^l = |h_s^l h_\varphi^l|$  and  $X_\varphi = \left| \sum_{l=1}^L |h_s^l h_\varphi^l| \right|^2$ . The PDF of  $X_\varphi^l$  can be given by [49]

$$f_{X_\varphi^l}(x) = 4 \sum_{u=0}^{\infty} \sum_{v=0}^{\infty} \frac{(\kappa+1)^{u+v+2} x^{u+v+1}}{(u!)^2 (v!)^2 e^{2\kappa} \kappa^{-u-v}} K_{u-v} [2x(\kappa+1)], \quad (6)$$

where  $K_x(\cdot)$  indicates the modified Bessel function of the second kind with order  $x$ . We can separately express the mean and variance of  $X_\varphi^l$  as

$$\mathbb{E}(X_\varphi^l) = \frac{\pi}{4(\kappa+1)} \left[ L_{\frac{1}{2}}(-\kappa) \right]^2, \quad (7)$$

and

$$\mathbb{D}(X_\varphi^l) = 1 - \frac{\pi^2}{16(\kappa+1)^2} \left[ L_{\frac{1}{2}}(-\kappa) \right]^4, \quad (8)$$

where  $L_{\frac{1}{2}}(x) = e^{\frac{x}{2}} \left[ (1-x) I_0\left(-\frac{x}{2}\right) - x I_1\left(-\frac{x}{2}\right) \right]$  is the Laguerre polynomial.

By applying Laguerre polynomial series [50, Eq. (2.76)], the PDF and CDF for  $X_\varphi$  are separately approximated as

$$f_{X_\varphi}(x) = \frac{x^{\frac{p_\varphi}{2}-1}}{2q_\varphi^{p_\varphi} \Gamma(p_\varphi)} e^{-\frac{\sqrt{x}}{q_\varphi}}, \quad (9)$$

and

$$F_{X_\varphi}(x) = \gamma\left(p_\varphi, \frac{\sqrt{x}}{q_\varphi}\right) \Gamma(p_\varphi)^{-1}, \quad (10)$$

where  $\gamma(a, x) = \int_0^x t^{a-1} e^{-t} dt$  is the lower incomplete Gamma function [51, Eq. (8.350.1)] and  $\Gamma(\cdot)$  is the gamma function [51, Eq. (8.310.1)],  $p_\varphi = \frac{K\mathbb{E}^2(X_\varphi^l)}{\mathbb{D}(X_\varphi^l)}$ ,  $q_\varphi = \frac{\mathbb{D}(X_\varphi^l)}{\mathbb{E}(X_\varphi^l)}$ .

2) *Thermal noise intensity*: Since  $\theta_l^\varphi$  can only be phase-aligned with the  $|\mathbf{h}_\varphi^H \Phi_\varphi \mathbf{h}_s|^2$ , the phase in each term of  $|\mathbf{h}_\varphi^H \Phi_\varphi \mathbf{n}_s|^2 = \eta_0 d_\varphi^{-\alpha} \sigma_s^2 \left| \sum_{l=1}^L h_\varphi^l \right|^2$  is considered to be randomly distributed. Let  $H = \sum_{l=1}^L h_\varphi^l$ , since  $H$  is obtained by adding up  $L$  independent identically distributed  $h_\varphi^l$ , it can be calculated as  $H = L\sqrt{\frac{\kappa}{\kappa+1}} + \sqrt{\frac{L}{\kappa+1}} \tilde{H}$ , where  $\tilde{H}$  follows a complex Gaussian distribution and  $\tilde{H} \sim \mathcal{CN}(0, 1)$ . We use the mean to characterize the channel power of  $H$ , which is expressed as  $\mathbb{E}(|H|^2) = L \left( \frac{L\kappa+1}{\kappa+1} \right)$ .

3) *User's location characteristics*: For the path-loss experienced by the users, the PDFs of  $d_\varphi$  can be obtained by using the fact that the locations of pairing users are stochastically distributed within ASTARS's serving area  $\mathbb{O}_D$ . In this case, the PDFs of  $d_r$  and  $d_t$  are written as [30]

$$f_{d_r}(x) = \frac{\partial}{\partial x} \int_0^x \int_0^\pi \frac{2r}{\pi D^2} dr d\theta = \frac{2x}{D^2}, \quad (11)$$

and

$$f_{d_t}(x) = \frac{\partial}{\partial x} \int_0^x \int_\pi^{2\pi} \frac{2r}{\pi D^2} dr d\theta = \frac{2x}{D^2}, \quad (12)$$

respectively.

### III. OUTAGE PROBABILITY

In this section, the outage behaviors of ASTARS-NOMA are evaluated by invoking the stochastic geometry. To be more specific, the closed-form outage probability expressions of  $U_r$  with pSIC/ipSIC and  $U_t$  are derived for ASTARS-NOMA. To acquire further insight, the asymptotic expressions of outage probability and diversity orders for  $U_r$  and  $U_t$  are obtained.

#### A. The $U_r$ 's Outage Probability

With the help of ASTARS,  $U_r$ , i.e., the user with strong channel conditions, needs to decode the information of  $U_t$ , and then decode its own signals. As a consequence, the  $U_r$  outage occurrences may be described as follows: 1) An outage event occurs when the signal  $x_t$  of  $U_t$  cannot be successfully decoded by  $U_r$ ; and 2) The signal  $x_t$  is successfully decoded, while the signal  $x_r$  of  $U_r$  fails to detect. Based on these explanations, the outage probability at  $U_r$  in ASTARS-NOMA networks is shown as

$$P_{out,r} = \Pr(\gamma_{r \rightarrow t} > \hat{\gamma}_t, \gamma_r < \hat{\gamma}_r) + \Pr(\gamma_{r \rightarrow t} < \hat{\gamma}_t), \quad (13)$$

where  $\hat{\gamma}_r = 2^{\hat{R}_r} - 1$  and  $\hat{\gamma}_t = 2^{\hat{R}_t} - 1$  separately represent the target SNR for decoding  $x_r$  and  $x_t$ . The corresponding target rates of  $U_r$  and  $U_t$  are defined as  $\hat{R}_r$  and  $\hat{R}_t$ , respectively. The outage probability expression of  $U_r$  with ipSIC for ASTARS-NOMA is illustrated in the following theorem.

**Theorem 1.** *Condition on  $a_t > \hat{\gamma}_t a_r$ , the closed-form expression of  $U_r$ 's outage probability with ipSIC for ASTARS-NOMA is written as*

$$P_{out,r}^{ipSIC} = \sum_{k=1}^K \sum_{u=1}^U \frac{\pi A_k (x_u+1)}{2U\Gamma(p_r)} \sqrt{1-x_u^2} \gamma \left\{ p_r, \frac{1}{q_r} \sqrt{\frac{\hat{\gamma}_r d_s^\alpha}{a_r P_s^{act}} \left[ \zeta \frac{\sigma_s^2}{\eta_0} + \frac{\chi_u^\alpha}{\eta_0^2} \left( \frac{\varepsilon y_k P_s^{act}}{\beta_r \lambda \sigma_{re}^{-2}} + \frac{\sigma_0^2}{\beta_r \lambda} \right) \right]} \right\}, \quad (14)$$

where  $\varepsilon = 1$ ,  $\zeta = L \left( \frac{L\kappa+1}{\kappa+1} \right)$ ,  $x_u = \cos \left( \frac{2u-1}{2U} \pi \right)$ ,  $\chi_u = \frac{(x_u+1)D}{2}$ ,  $y_k$  is the  $k$ -th zero point of Laguerre polynomial  $L_K(y_k)$  and the  $k$ -th weight is expressed as  $A_k = \frac{(K!)^2 y_k}{[L_{K+1}(y_k)]^2}$ . In addition, a trade-off between complexity and accuracy is also guaranteed by the parameters  $K$  and  $U$ .

*Proof.* See Appendix A. □

**Remark 1.** If  $a_t < \hat{\gamma}_t a_r$ , and by substituting (3) and (4) into (13), the expression of  $U_r$ 's outage probability with ipSIC can be written as

$$P_{out,r}^{ipSIC} = \Pr \left[ |\mathbf{h}_r^H \Phi_r \mathbf{h}_s|^2 \geq \frac{\partial}{P_s^{act}} \left( |\mathbf{h}_r^H \Phi_r \mathbf{n}_s|^2 + \frac{\sigma_0^2}{\beta_r \lambda} \right) \right], \quad (15)$$

where  $\partial = \frac{\hat{\gamma}_t}{(a_t - \hat{\gamma}_t a_r)}$ . Due to condition  $a_t < \hat{\gamma}_t a_r$ , the right side of the inequality (15) is less than zero, making the inequality always hold. At this time, the outage probability of  $U_r$  with ipSIC will always equal to one.

**Corollary 1.** For case  $\varepsilon = 0$ , the closed-form expression of  $U_r$ 's outage probability with pSIC for ASTARS-NOMA is written as

$$P_{out,r}^{pSIC} = \sum_{u=1}^U \gamma \left[ p_r, \frac{1}{q_r} \sqrt{\frac{\hat{\gamma}_r d_s^\alpha}{a_r P_s^{act}} \left( \frac{\chi_u^\alpha \sigma_0^2}{\eta_0^2 \beta_r \lambda} + \zeta \frac{\sigma_s^2}{\eta_0} \right)} \right] \frac{\pi (x_u+1)}{2U\Gamma(p_r)} \sqrt{1-x_u^2}. \quad (16)$$

### B. The $U_t$ 's Outage Probability

The following can be applied to indicate the outage occurrence at  $U_t$ : the SINR of decoded signal  $x_t$  is lower the target SINR. The corresponding outage probability is shown as

$$P_{out,t} = \Pr(\gamma_t < \hat{\gamma}_t). \quad (17)$$

**Theorem 2.** Condition on  $a_t > \hat{\gamma}_t a_r$ , the closed-form expression of  $U_t$ 's outage probability for ASTARS-NOMA is written as

$$P_{out,t} = \sum_{u=1}^U \gamma \left[ p_t, \sqrt{\frac{\partial d_s^\alpha q_t^{-2}}{P_s^{act}} \left( \frac{y_u^\alpha \sigma_0^2}{\eta_0^2 \beta_t \lambda} + \zeta \frac{\sigma_s^2}{\eta_0} \right)} \right] \frac{\pi (x_u+1)}{2U\Gamma(p_t)} \sqrt{1-x_u^2}, \quad (18)$$

where  $\partial = \frac{\hat{\gamma}_t}{(a_t - \hat{\gamma}_t a_r)}$ . Similar to **Remark 1**, if  $a_t < \hat{\gamma}_t a_r$ , the outage probability of  $U_t$  will always equal to one.

*Proof.* By substituting (5) into (17), the outage probability expression of  $U_t$  is further expressed as

$$P_{out,t} = \Pr \left[ |\mathbf{h}_t^H \Phi_t \mathbf{h}_s|^2 < \partial \left( \frac{|\mathbf{h}_t^H \Phi_t \mathbf{n}_s|^2}{P_s^{act}} + \frac{\beta_t^{-1} \sigma_0^2}{P_s^{act} \lambda} \right) \right]. \quad (19)$$

By configuring the reflection phase-shift to align the phases of cascaded channels, the above expression can be rewritten as

$$P_{out,t} = \Pr \left[ \left| \sum_{l=1}^L h_s^l h_t^l \right|^2 \leq \frac{\partial d_s^\alpha}{P_s^{act}} \left( \frac{\zeta \sigma_s^2}{\eta_0} + \frac{d_t^\alpha \sigma_0^2}{\eta_0^2 \beta_t \lambda} \right) \right]. \quad (20)$$

The following procedures resemble those in Appendix A. The proof is completed.  $\square$

**Proposition 1.** *When an outage occurs for at least one user in the system, it is considered as a system outage event. Hence, the ASTARS-NOMA's system outage probability with pSIC/ipSIC is written as*

$$P_{NOMA,\tau}^{ASTARS} = 1 - (1 - P_{out,r}^\tau) (1 - P_{out,t}), \quad (21)$$

where  $\tau \in \{ipSIC, pSIC\}$ .  $P_{out,r}^{ipSIC}$ ,  $P_{out,r}^{pSIC}$  and  $P_{out,t}$  is given by (14), (16) and (18), respectively.

### C. Diversity Analysis

The diversity order is an essential performance metric in wireless networks, which determines the robustness and fading resistance of networks. Specifically, a system with a larger diversity order means that the outage probability decays faster and it is more robust to fading [52], particularly at high SNR. The analysis of diversity order provides a basis for optimizing networks performance and designing more efficient diversity mechanisms. The expression of diversity order is shown as

$$D_{order} = - \lim_{P_s^{act} \rightarrow \infty} \frac{\log (P_{out}^\infty (P_s^{act}))}{\log P_s^{act}}, \quad (22)$$

where  $P_{out}^\infty (P_s^{act})$  denotes the asymptotic expression of outage probability within high SNR region ( $P_s^{act} \rightarrow \infty$ ).

The expression for the asymptotic outage probability of  $U_r$  with ipSIC can be directly derived from (14), and it is provided by the following corollary.

**Corollary 2.** Condition on  $P_s^{act} \rightarrow \infty$ , an asymptotic expression of  $U_r$ 's outage probability with ipSIC for ASTARS-NOMA is written as

$$P_{out,r}^{ipSIC,\infty} = \sum_{k=1}^K \sum_{u=1}^U \frac{\pi A_k \chi_u}{2U\Gamma(p_r)} \gamma \left( p_r, \sqrt{\frac{y_k \hat{\gamma}_r d_s^\alpha \chi_u^\alpha \sigma_{re}^2}{\eta_0^2 a_r \beta_r \lambda q_r^2}} \right), \quad (23)$$

where  $\chi_u = \sqrt{1 - x_u^2} (x_u + 1)$ .

**Remark 2.** As can be observed that the outage probability of  $U_r$  with ipSIC is almost constant under the assumptions of  $P_s^{act} \rightarrow \infty$ , i.e., there is an error floor for the outage probability achieved for  $U_r$  with ipSIC. By substituting (23) into (22), the diversity order of  $U_r$  with ipSIC can be calculated as zero. This is attributed to the effect of residual interference generated by the ipSIC scheme on networks outage performance.

For  $U_r$  with pSIC and  $U_t$ , the precise outage probability diversity orders can be calculated by employing the Laplace transform.

**Corollary 3.** Condition on  $P_s^{act} \rightarrow \infty$ , an asymptotic expression of  $U_r$ 's outage probability with pSIC for ASTARS-NOMA is given by

$$P_{out,r}^{pSIC,\infty} = \pi \sum_{u=1}^U \frac{(x_u + 1) \sqrt{1 - x_u^2}}{2U (2L)! \Lambda^L} \left[ {}_2F_1 \left( 2, \frac{1}{2}; \frac{5}{2}; 1 \right) \right]^L \left[ \frac{\hat{\gamma}_r d_s^\alpha}{a_r P_s^{act}} \left( \frac{\chi_u^\alpha \sigma_0^2}{\eta_0^2 \beta_r \lambda} + \zeta \frac{\sigma_s^2}{\eta_0} \right) \right]^L, \quad (24)$$

where  $\Lambda = \frac{3e^{2\kappa}}{16(1+\kappa)^2}$  and  ${}_2F_1(\cdot, \cdot; \cdot; \cdot)$  stands for the ordinary hypergeometric function [51, Eq. (9.100)].

*Proof.* See Appendix B. □

**Remark 3.** The  $U_r$ 's diversity order with pSIC can be calculated as  $L$  by substituting (24) into (22), which is proportional to the number of ASTARS elements  $L$ . The  $U_r$ 's asymptotic outage probability under the pSIC scheme is an oblique line rather than a constant. This indicates that the reflection user  $U_r$  with pSIC for ASTARS-NOMA is able to achieve a diversity order of  $L$ , which is the maximal diversity for the considered scenario.

**Corollary 4.** Condition on  $P_s^{act} \rightarrow \infty$ , an asymptotic expression of  $U_t$ 's outage probability for ASTARS-NOMA is written as

$$P_{out,t}^\infty = \pi \sum_{u=1}^U \frac{(x_u+1) \sqrt{1-x_u^2}}{2^U (2L)! \Lambda^L} \left[ {}_2F_1 \left( 2, \frac{1}{2}; \frac{5}{2}; 1 \right) \right]^L \left[ \frac{\hat{\gamma}_t d_s^\alpha \eta_0^{-2}}{(a_t - \hat{\gamma}_t a_r)} \left( \frac{y_u^\alpha \sigma_0^2}{\beta_t \lambda P_s^{act}} + \zeta \frac{\eta_0 \sigma_s^2}{P_s^{act}} \right) \right]^L. \quad (25)$$

*Proof.* The following procedures resemble those in Appendix B.  $\square$

**Remark 4.** The  $U_t$ 's diversity order is calculated as  $L$  by substituting (25) into (22), which is proportional to the numbers of ASTARS elements. This indicates that  $U_t$  of ASTARS-NOMA is also able to achieve the full diversity order.

#### D. Delay-limited Transmission

System throughput in delay-limited transmission situations depends on the outage probability at a target data rate [53]. When an outage occurs during data transmission, it means that the data transmission fails and a retransmission is required. At this moment, the system throughput of ASTARS-NOMA with pSIC/ipSIC schemes in delay-limited transmission mode are defined as

$$R_\tau^{limited} = (1 - P_{out,r}^\tau) \hat{R}_r + (1 - P_{out,t}) \hat{R}_t, \quad (26)$$

where  $P_{out,r}^{ipSIC}$ ,  $P_{out,r}^{pSIC}$  and  $P_{out,t}$  are obtained from (14), (16) and (18), respectively.

## IV. ERGODIC DATA RATE ANALYSIS

This section analyzes the ergodic data rate of  $U_t$  and  $U_r$  with pSIC/ipSIC to reveal the data transmission rate and capability of ASTARS-NOMA networks. The definition of ergodic data rate is shown as

$$R^{erg} = \mathbb{E} [\log_2 (1 + \gamma_\varphi)], \quad (27)$$

which indicates that the high ergodic data rate achieves high channel capacity. On this basis, we further derive the asymptotic expressions of ergodic data rate for  $U_r$  with pSIC/ipSIC and  $U_t$ . Furthermore, the multiplexing gains for  $U_r$  and  $U_t$  are discussed in detail.

### A. The Ergodic Data Rate of ASTARS-NOMA Networks

Assuming that  $U_r$  can effectively detect information  $x_t$  by using the ipSIC method, the expression of  $U_r$ 's ergodic data rate with ipSIC is then obtained as the following theorem.

**Theorem 3.** *Conditioned on the stochastic geometry model and cascade Rician fading channels, a closed-form expression of  $U_r$ 's ergodic data rate with ipSIC for ASTARS-NOMA is written as*

$$R_{r,ipSIC}^{erg} = \sum_{q=1}^Q \sum_{k=1}^K \sum_{u=1}^U \frac{\pi \ln \left[ 1 + (x_q \vartheta^{-1})^2 \right] A_k A_q (x_u + 1)}{2U \ln 2 \Gamma(p_r) x_q^{1-p_r}}, \quad (28)$$

where  $\vartheta = \frac{1}{q_r} \sqrt{\frac{d_s^\alpha}{a_r P_s^{act}} \left[ \zeta \frac{\sigma_s^2}{\eta_0} + \frac{\chi_u^\alpha}{\eta_0^2} \left( \frac{\varepsilon y_k P_s^{act}}{\beta_r \lambda \sigma_r^{-2}} + \frac{\sigma_0^2}{\beta_r \lambda} \right) \right]}$  and  $Q$  is the parameter that guarantee a trade-off between complexity and accuracy of Gauss-Laguerre quadra.

*Proof.* See Appendix C. □

**Corollary 5.** *For case  $\varepsilon = 0$ , a closed-form expression of  $U_r$ 's ergodic data rate with pSIC for ASTARS-NOMA is written as*

$$R_{r,pSIC}^{erg} = \sum_{q=1}^Q \sum_{u=1}^U \ln \left( 1 + \frac{a_r \beta_r \lambda (x_q q_r \eta_0)^2 P_s^{act}}{d_s^\alpha (\chi_u^\alpha \sigma_0^2 + \zeta \eta_0 \beta_r \lambda \sigma_s^2)} \right) \frac{\pi A_q (x_u + 1) \sqrt{1 - x_u^2}}{2U \ln 2 \Gamma(p_r) x_q^{1-p_r}}. \quad (29)$$

**Theorem 4.** *Conditioned on the stochastic geometry model and cascade Rician fading channels, a closed-form expression of  $U_t$ 's ergodic data rate for ASTARS-NOMA is written as*

$$R_t^{erg} = \frac{\pi a_t}{2N a_r \ln 2} \sum_{n=1}^N \frac{\sqrt{1 - x_n^2}}{1 + y_n} \left\{ 1 - \sum_{u=1}^U \frac{\pi \chi_u}{2U \Gamma(p_t)} \gamma \left[ p_t, \sqrt{\frac{y_n d_s^\alpha q_t^{-2}}{P_s^{act} (a_t - y_n a_r)} \left( \frac{y_u^\alpha \sigma_0^2}{\eta_0^2 \beta_t \lambda} + \zeta \frac{\sigma_s^2}{\eta_0} \right)} \right] \right\}, \quad (30)$$

where  $y_n = \frac{(x_n + 1)a_t}{2a_r}$  and  $x_n = \cos\left(\frac{2n-1}{2U}\pi\right)$ .

*Proof.* See Appendix D. □

### B. Multiplexing Gains Analysis

We now analyze the multiplexing gains of ASTARS-NOMA networks at high SNRs ( $P_s^{act} \rightarrow \infty$ ) to reveal the variation of the ergodic data rate with transmit power [54], which is defined as

$$S = \lim_{P_s^{act} \rightarrow \infty} \frac{\log(R_\infty^{erg}(P_s^{act}))}{\log P_s^{act}}, \quad (31)$$

where  $R_\infty^{erg}(P_s^{act})$  is the asymptotic expression of the ergodic data rate within high SNR areas.

1) *The  $U_r$ 's multiplexing gain with ipSIC:* Based on (28), when  $P_s^{act} \rightarrow \infty$  the asymptotic expression of  $U_r$ 's ergodic data rate with ipSIC for ASTARS-NOMA is written as

$$R_{r,ipSIC}^{erg,\infty} = \sum_{q=1}^Q \sum_{k=1}^K \sum_{u=1}^U \ln \left[ 1 + (\eta_0 x_q q_r)^2 \frac{\lambda \beta_r a_r}{d_s^\alpha \chi_u^\alpha y_k \sigma_{re}^2} \right] \frac{\pi A_k A_q (x_u + 1)}{2U \ln 2 \Gamma(p_r)} x_q^{p_r - 1}. \quad (32)$$

**Remark 5.** *By substituting (32) into (31), a multiplexing gain of zero for  $U_r$  with ipSIC is obtained. It implies that even when the  $P_s^{act}$  is sufficiently high, the ergodic data rate will not increase.*

2) *The  $U_r$ 's multiplexing gain with pSIC:* We obtain an upper bound on the ergodic data rate by invoking Jensen's inequality, which is written as

$$R_{r,pSIC}^{erg} = \mathbb{E}[\log_2(1 + \gamma_r)] \leq \log_2[1 + \mathbb{E}(\gamma_r)]. \quad (33)$$

Based on the above inequality, when  $P_s^{act} \rightarrow \infty$  an upper bound expression of  $U_r$ 's ergodic data rate with pSIC for ASTARS-NOMA networks is written as

$$R_{r,erg}^{bound} = \log \left\{ 1 + \frac{\Xi L \lambda P_s^{act} [D(X_r^l) + LE^2(X_r^l)]}{d_s^\alpha [\lambda \beta_r \eta_0 \sigma_s^2 \zeta (2 + \alpha) + 2D^{2+\alpha} \sigma_0^2]} \right\}, \quad (34)$$

where  $\Xi = \eta_0^2 a_r \beta_r (2 + \alpha)$ .

**Remark 6.** *The multiplexing gain for  $U_r$  with pSIC is equal to one by inserting (34) into (31), which is due to the limitation of power allocation factors ratio at high SNRs.*

3) *The  $U_t$ 's multiplexing gain:* When  $P_s^{act} \rightarrow \infty$  the asymptotic ergodic data rate expression of  $U_t$  for ASTARS-NOMA networks can be obtained directly from (30) as

$$R_t^{erg,\infty} = \frac{\pi a_t}{2N a_r \ln 2} \sum_{n=1}^N \frac{\sqrt{1 - x_n^2}}{1 + y_n}. \quad (35)$$

**Remark 7.** *The multiplexing gain for  $U_t$  is equal to zero, by inserting (35) into (31), which has the same conclusion as in Remark 5.*

### C. Delay-tolerant Transmission

The data transmission is capped at the ergodic data rate in delay-tolerant transmission situations because the codeword can experience all channel realizations [53]. In this scenario, the system throughput of ASTARS-NOMA with pSIC/ipSIC schemes in delay-tolerated transmission mode are defined as

$$R_{\vartheta}^{tolerant} = R_{r,\tau}^{erg} + R_t^{erg}, \quad (36)$$

TABLE I: Simulation Parameters for ASTARS-NOMA networks.

|   |   |
|---|---|
| Monte Carlo simulations repeated                | $10^6$ iterations   |
| Rician factor                                   | $\kappa = -5$ dB  |
| Amplification factor                            | $\lambda = 5$   |
| Number of ASTARS elements                       | $L = 10$  |
| Coverage radius of ASTARS                       | $D = 35$ m  |
| Distance from BS to ASTARS                      | $d_s = 50$ m  |
| Amplitude coefficients of ASTARS elements       | $\beta_r = 0.7, \beta_t = 0.3$                                    |
| The power allocation factors of $U_r$ and $U_t$ | $a_r = 0.3, a_t = 0.7$  |
| Noise power                                     | $\sigma_s^2 = -70$ dBm<br>$\sigma_0^2 = \sigma_{r_e}^2 = -90$ dBm |
| Pass loss factors                               | $\alpha = 2$<br>$\eta_0 = -30$ dB                                 |
| Target data rates for $U_r$ and $U_t$           | $\hat{R}_r = 1$ BPCU<br>$\hat{R}_t = 1$ BPCU                      |

where  $R_{r,ipSIC}^{erg}$ ,  $R_{r,pSIC}^{erg}$  and  $R_t^{erg}$  can be obtained from (28), (29) and (30).

## V. SIMULATION RESULTS

This section provide the computer simulation results to verify the correctness of the theoretical formulas in Sections III and IV. The simulation settings used, unless otherwise specified, are displayed in Table I. The complexity-accuracy trade-off parameters  $K$ ,  $Q$  and  $U$  are set to  $10^3$ . To highlight the performance of ASTARS-NOMA networks, the ARIS-NOMA, ASTARS-OMA and PSTARS-NOMA networks are selected as benchmarks. In particular, the total power budgets of ASTARS and PSTARS-aided networks are respectively given by  $Q_{tot}^{act} = P_s^{act} + P_r^{act} + L(P_c + P_d)$  and  $Q_{tot}^{pas} = P_s^{pas} + LP_c$  [37] [39], where  $P_r^{act}$  is the output signal power of ASTARS/ARIS, the power used by the phase shift control circuit in each active element is  $P_c = -20$  dBm and the direct current bias power used by the amplifier placed in each ASTARS/ARIS element is indicated as  $P_d = -20$  dBm. To achieve fair comparisons,  $Q_{tot}^{act}$  is set to be the same as  $Q_{tot}^{pas}$ . Moreover, in ARIS-NOMA networks, to obtain  $360^\circ$  coverage, we employ a surface made up of one transmit-only RIS and one reflect-only RIS [55]. It's also important to note that ASTARS-OMA networks employ time division multiple access, which takes twice as long as NOMA for serving the two users.

### A. Outage Probability

In Fig. 2(a), we plot the outage probability of  $U_r$  and  $U_t$  versus the system power budget. The outage probability curves of  $U_t$  and  $U_r$  with pSIC/ipSIC curves are plotted by (14), (16)

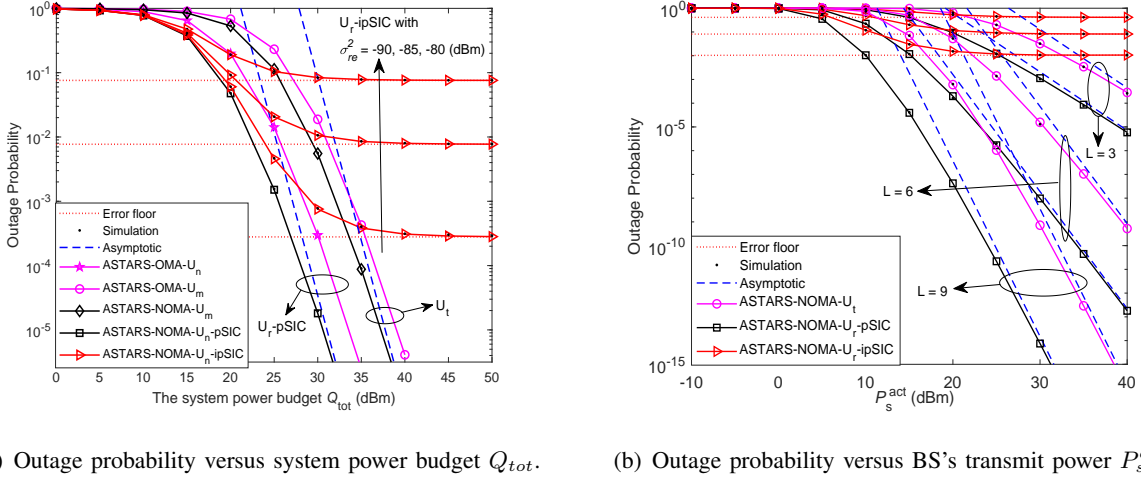
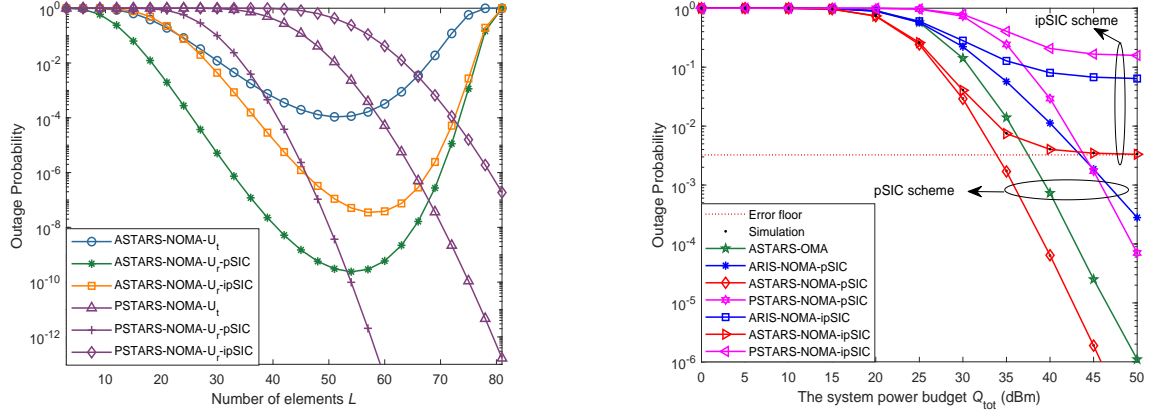


Fig. 2: Outage probability of ASTARS-NOMA networks.

and (18), respectively. This figure demonstrates that the obtained analytical expressions match the simulation results exactly, which validates the accuracy of the analytical methods applied. The blue dotted lines for asymptotic outage probability are plotted based on (23), (24) and (25), respectively. They perfectly match the outage probability curves of ASTARS-NOMA within high SNR region, proving that our asymptotic approach is accurate. One phenomenon is that the outage performance of  $U_r$  with pSIC and  $U_t$  for ASTARS-NOMA outperforms that of ASTARS-OMA, which is due to the following two reasons. 1) NOMA is able to achieve better fairness in outage performance between paring users; and 2) The performance of ASTAR-NOMA can be further enhanced by the better compatibility between ASTARS and NOMA. Another phenomenon is that, after  $Q_{tot}$  exceeds 30 dBm, the outage performance of  $U_r$  with ipSIC for ASTARS-NOMA is worse than that of ASTARS-OMA. In high SNR area, it converges to an error floor. This is attributed that the  $U_r$  in ASTARS-NOMA networks suffers from residual interference caused by ipSIC, which confirms the conclusions made in **Remark 2**. Moreover, Fig. 2(b) displays the outage probability of  $U_r$  and  $U_t$  for ASTARS-NOMA networks versus transmit power of BS under  $L = \{3, 6, 9\}$ . The figure shows that as the number of ASTARS elements rises, the outage probability falls and its slope rises. This phenomenon is caused by the fact that the diversity orders of  $U_t$  and  $U_r$  with pSIC are proportional to the number of ASTARS elements, which confirms the conclusions made in **Remark 3** and **Remark 4**.

In Fig. 3(a), we plot the outage probability of ASTARS-NOMA versus number of ASTARS



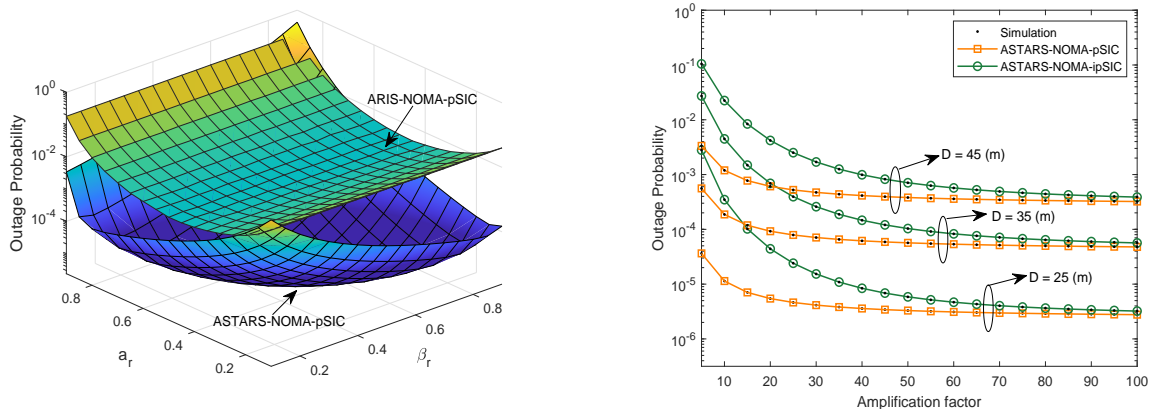
(a) Outage probability versus number of ASTARS/ARIS elements (b) System outage probability versus system power budget  $Q_{tot}$ .  $L$ , with  $Q_{tot}^{act} = Q_{tot}^{pas} = 20$  dBm,  $\lambda = 10$  and  $\sigma_s^2 = -30$  dBm.

Fig. 3: Outage probability of ASTARS-NOMA networks.

elements  $L$ , with  $Q_{tot}^{act} = Q_{tot}^{pas} = 20$  dBm,  $\lambda = 10$  and  $\sigma_s^2 = -30$  dBm. As can be observed that with ASTARS elements increase, the outage probability first decreases and then gradually increases. This trend can be attributed to the complex interactions between various factors. On the one hand, the introduction of more ASTARS elements can enhance the spatial degrees of freedom and thus reduce the outage probability. This is because that the increased degrees of freedom enable a more efficient use of spatial domain, resulting in better signal quality and stronger channel gains. On the other hand, using too many ASTARS elements can lead to a large amount of thermal noise, which severely hinders the user's ability to decode the signal. This counteracts the channel gains generated by spatial degrees of freedom and leads to a surge in outage probability. Hence, the optimization of ASTARS-NOMA networks is a balance between the numbers of active component and the spatial degrees of freedom, with the ultimate goal of minimizing outage probability.

Fig. 3(b) displays the system outage probability of ASTARS-NOMA and different benchmarks versus the system power budget. As can be shown that the outage performance of ASTARS-NOMA perform better than the PSTARS-NOMA. This can be interpreted that the ASTARS elements allocate a portion of power budget to amplify the input radio signals, which enhances the received SNR at paring users. This also confirms that ASTARS is an effective technology for combating multiplicative fading loss. One occurrence is that ASTARS-NOMA achieves better

outage performance than ARIS-NOMA. In addition, the outage curves of ASTARS-NOMA are steeper than the OMA ones. This can be explained by the fact that ASTARS is able to achieve a better diversity order than ARIS.



(a) System outage probability versus reflection amplitude coefficient and power allocation factor, with  $P_s^{act} = 20$  dBm. (b) Outage probability versus amplification factor  $\lambda$ , with  $P_s^{act} = 25$  dBm and  $\sigma_s^2 = -50$  dBm.

Fig. 4: Outage probability of ASTARS-NOMA networks.

In Fig. 4(a), we show the system outage probability of ASTARS-NOMA versus reflection amplitude coefficient and power allocation factor under  $Q_{act} = 20$  dBm. The curved surface for outage probability of ASTARS-NOMA is plotted according to (21). Due to the effects of both amplitude coefficients and power allocation factors, the curved surface for outage probability of ASTARS-NOMA takes on a valley-like shape. This suggests the existence of a solution that satisfies the minimum system outage probability for the given parameter. Additionally, it can be shown that by adjusting  $a_r$ , the ARIS-NOMA's outage probability can be reduced. However, in most cases of parameter setting, the outage performance of ARIS-NOMA is inferior to that of ASTARS-NOMA. This is because that ASTARS can introduce more spatial degrees of freedom for NOMA networks, which enhances the outage performance. It is worth noting that when with some extreme parameter choices, such as  $\beta_r = 0.1$  and  $a_r = 0.1$ , the performance of ASTARS-NOMA networks may be even worse than that of ARIS-NOMA networks. This indicates that optimizing the amplitude coefficients and power allocation factors is essential to reducing the outage probability of ASTARS-NOMA.

In Fig. 4(b), we plot the system outage probability of ASTARS-NOMA versus amplification

factor  $\lambda$ , with  $P_s^{act} = 25$  dBm and  $\sigma_s^2 = -50$  dBm. One phenomenon is that the outage probability of ASTARS-NOMA first reduces dramatically as the amplification factor steadily rises and then tends to stabilize. This is due to the fact that the larger amplification factors helps to improve the users' received SNR, thus enhancing the outage performance. However, while increasing the received signal strength at the users, also introduces a large amount of thermal noise, which interferes with the decoding of user signals. As the amplification factor increases, a balance is achieved between the gain of the enhanced signal and the loss of the enhanced noise such that the outage probability remains constant. Another observation is that reducing the deployment range of users improves outage performance. This is because that a smaller deployment range diminishes the effect of path loss on the ASTARS-NOMA's outage probability.

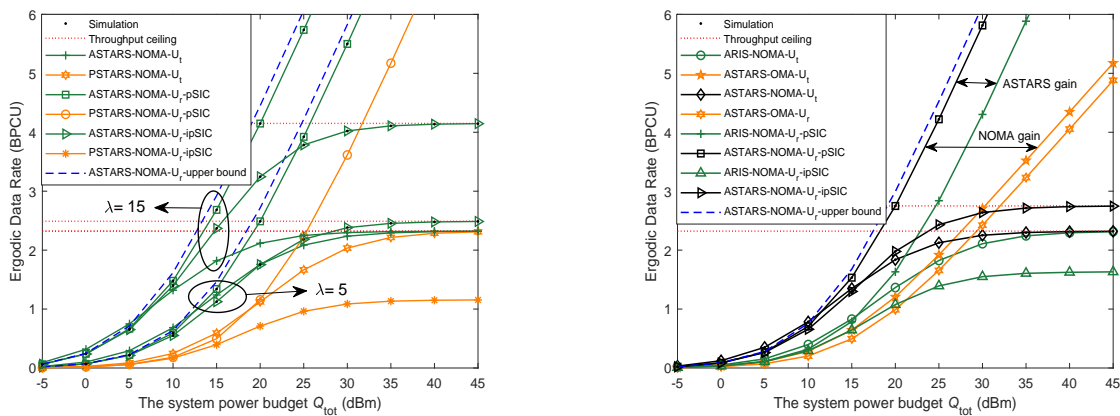
### B. Ergodic Data Rate

In Fig. 5(a), we present ergodic data rate of ASTARS-NOMA and PSTARS-NOMA versus system power budget with  $a_r = 0.2$ ,  $a_t = 0.8$ . The ergodic data rate curves for ASTARS-NOMA networks are drawn from (28), (29) and (30), respectively. According to (32), (34) and (35), the asymptotic ergodic data rates are illustrated. This figure indicates that the  $U_t$ 's ergodic data rate converges towards the upper limit of the throughput, resulting in *zero* high SNR slope. The ergodic data rate of ipSIC stops increasing with a rise in transmit power at high SNRs due to the effects of residual interference, which in accordance with the discussion in **Remark 5**. One phenomenon is that the  $U_r$ 's ergodic data rates with pSIC/ipSIC of ASTARS-NOMA are higher than those of PSTARS-NOMA. This is due to the fact that ASTARS is able to increase the strength of users' received signals, which further increase the average data transmission rate of networks over an extended period. Another phenomenon is that the ergodic data rates of ASTARS-NOMA with a larger power amplification factor is more efficient. This suggests that increasing the power amplification factor can enhance the receiving SNR and thus improve the ergodic data rate of ASTARS-NOMA.

Fig. 5(b) compares the ergodic data rates of ASTARS-NOMA with ARIS-NOMA and ASTARS-OMA. This figure indicates that the  $U_r$ 's ergodic data rate with pSIC/ipSIC of ASTARS-NOMA outperform that of ARIS-NOMA and ASTARS-OMA. For the OMA transmission, it takes twice as long to serve two users as NOMA transmission. As a result, the slope of OMA transmission is only half of that of NOMA transmission, which is the reason for its lower ergodic data rate. The reason why ARIS-NOMA networks have lower ergodic data rate compared to ASTARS-NOMA

networks is that they cannot provide the same spatial degrees of freedom as ASTARS networks do. Another phenomenon is that the ergodic data rate of  $U_t$  for ASTARS-NOMA outperforms ARIS-NOMA at low SNRs, while they reach the same upper limit of rate within high SNR region. This can be explained by using the conclusion of **Remark 7** that the upper limit of  $U_t$ 's ergodic data rate in the NOMA network is related to the power allocation factors.

Additionally, Fig. 6 plots the ergodic data rate of ASTARS-NOMA networks versus system power budget with different path loss exponents, i.e.,  $\alpha$ . In ASTARS-NOMA networks,  $\alpha$  is a parameter to describe the signal power attenuation as it propagates through the wireless channels. A few real-world channel models are to be adopted, depending on the choice of  $\alpha$ . For example,  $\alpha = 2$  denotes the free space propagation case,  $\alpha = 2.5$  denotes the scenario with obstacles and  $\alpha = 3$  denotes the urban cellular networks. One can observe that as  $\alpha$  increases, the channel conditions of ASTARS-NOMA networks become progressively worse, resulting in a deterioration of outage performance. This indicates that a reasonable  $\alpha$  should be selected when studying the ASTARS-NOMA networks in different practical scenarios.



(a) Ergodic data rate versus system power budget  $Q_{tot}$  with  $a_r = 0.2$ ,  $a_t = 0.8$ . (b) Ergodic data rate versus system power budget  $Q_{tot}$  with  $a_r = 0.2$ ,  $a_t = 0.8$ .

Fig. 5: Ergodic data rate of ASTARS-NOMA networks.

### C. System Throughput

In Fig. 7(a), we present the system throughput of ASTARS-NOMA with pSIC/ipSIC versus system power budget in the delay-limited transmission mode. According to (26), the system

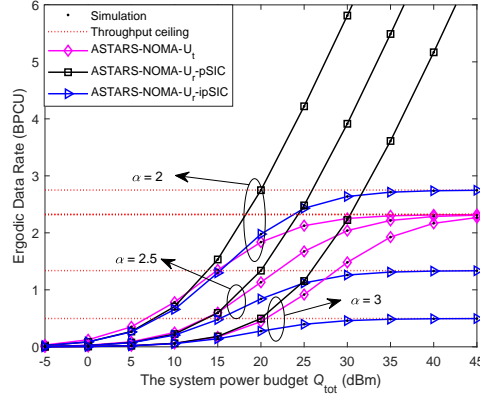
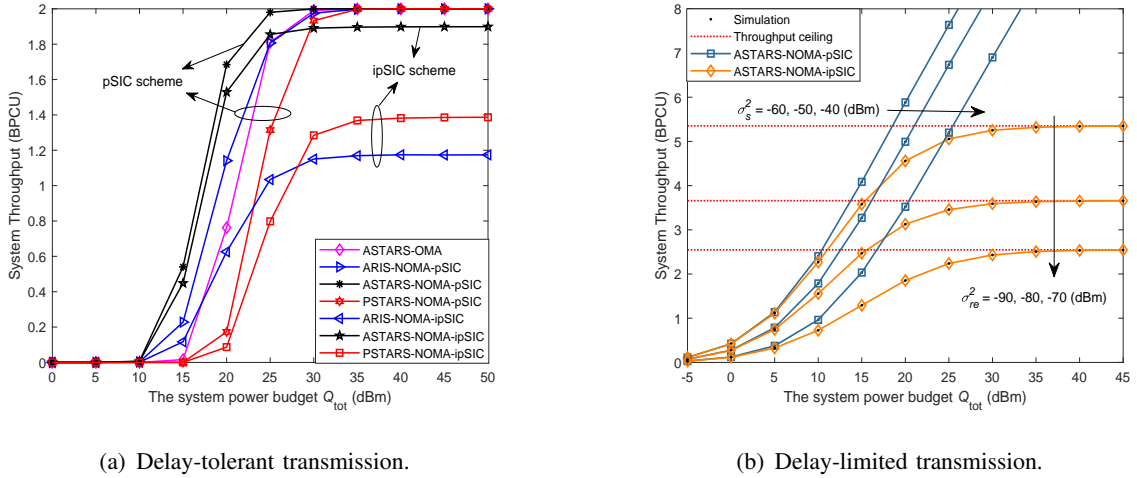


Fig. 6: Ergodic data rate versus system power budget  $Q_{tot}$  with  $\alpha_r = 0.2$ ,  $\alpha_t = 0.8$ .



(a) Delay-tolerant transmission.

(b) Delay-limited transmission.

Fig. 7: System throughput versus system power budget  $Q_{tot}$ .

throughput curves of ASTARS-NOMA with pSIC/ipSIC are drawn. One phenomenon is that the system throughput of ASTARS-NOMA outperform other comparison baselines under pSIC scheme. This is attributed to the fact that outage probability under delay-limited transmission model determines the throughput of ASTARS-NOMA networks. It can also be seen that the NOMA networks with ipSIC fail to reach the target rate even when the transmit power is large. This is due to the fact that residual interference limits the performance gains from increasing transmit power at high SNRs.

Fig. 7(b) shows the system throughput of ASTARS-NOMA versus system power budget in

the delay-tolerant transmission model, with  $a_r = 0.2$ ,  $a_t = 0.8$  and  $\alpha = 2.3$ . According to (36), the system throughput curves of ASTARS-NOMA with pSIC/ipSIC schemes are shown. One phenomenon is that the system throughput ceiling of ASTARS-NOMA under ipSIC scheme increases as residual interference strength diminishes. Another phenomenon is that reducing the noise intensity generated by active devices can improve the system throughput of ASTARS-NOMA with pSIC. This indicates that the design of low-power and low-interference hardware architecture is essential to improve the performance of ASTARS-NOMA.

## VI. CONCLUSION

In this article, we have studied the novel ASTARS-NOMA networks with randomly deployed users, which can mitigate the multiplicative fading loss and achieve full-space smart radio environments. Specifically, we have obtained analytical expressions of outage probability and ergodic data rate for ASTARS-NOMA networks with pSIC/ipSIC scheme. To gain further insights, the asymptotic expressions of outage probability and ergodic data rate were also obtained within high SNR region. On this basis, we have analyzed the diversity orders and multiplexing gains for paring users. Simulation results demonstrated that the performance of ASTARS-NOMA outperforms the PSTARS-NOMA, ARIS-NOMA and ASTARS-OMA for the same power consumption. For hardware configuration, the ASTARS-NOMA networks require an appropriate power amplification factors and number of ASTARS elements to ensure that the thermal noise interference is within a reasonable range.

### APPENDIX A: PROOF OF THEOREM 1

The top of the next page displays the expression of  $U_r$ 's outage probability with ipSIC by substituting (3) and (4) into (13). After combining the probability events, (A.1) can be simplified to

$$P_{out,r}^{ipSIC} = \Pr \left[ |\mathbf{h}_r^H \Phi_r \mathbf{h}_s|^2 \leq \frac{\hat{\gamma}_r}{a_r P_s^{act}} \left( |\mathbf{h}_r^H \Phi_r \mathbf{n}_s|^2 + \frac{\varepsilon |h_{re}|^2}{\beta_r \lambda} P_s^{act} + \frac{\sigma_0^2}{\beta_r \lambda} \right) \right]. \quad (\text{A.2})$$

With help of the topics discussed in Section II-B2,  $U_r$ 's outage probability with ipSIC can be further calculated as

$$P_{out,r}^{ipSIC} = \Pr \left\{ \underbrace{\left| \sum_{l=1}^L |h_s^l h_r^l| \right|^2}_{X_r} \leq \frac{\hat{\gamma}_r d_s^\alpha}{a_r \eta_0^2} \left[ \zeta \frac{\eta_0 \sigma_s^2}{P_s^{act}} + \underbrace{d_r^\alpha}_{Z} \left( \frac{\varepsilon}{\beta_r \lambda} \underbrace{|h_{re}|^2}_Y + \frac{\sigma_0^2}{\beta_r \lambda P_s^{act}} \right) \right] \right\}, \quad (\text{A.3})$$

$$\begin{aligned}
P_{out,r}^{ipSIC} &= \Pr \left[ \frac{a_t \lambda \beta_r P_s^{act} |\mathbf{h}_r^H \Phi_r \mathbf{h}_s|^2}{a_r \lambda \beta_r P_s^{act} |\mathbf{h}_r^H \Phi_r \mathbf{h}_s|^2 + \lambda \beta_r |\mathbf{h}_r^H \Phi_r \mathbf{n}_s|^2 + \sigma_0^2} \leq \hat{\gamma}_t \right] \\
&+ \left[ \frac{a_t \lambda \beta_r P_s^{act} |\mathbf{h}_r^H \Phi_r \mathbf{h}_s|^2}{a_r \lambda \beta_r P_s^{act} |\mathbf{h}_r^H \Phi_r \mathbf{h}_s|^2 + \lambda \beta_r |\mathbf{h}_r^H \Phi_r \mathbf{n}_s|^2 + \sigma_0^2} > \hat{\gamma}_t, \frac{a_r \lambda \beta_r P_s^{act} |\mathbf{h}_r^H \Phi_r \mathbf{h}_s|^2}{\lambda \beta_r |\mathbf{h}_r^H \Phi_r \mathbf{n}_s|^2 + \varepsilon |h_{re}|^2 P_s^{act} + \sigma_0^2} \leq \hat{\gamma}_r \right].
\end{aligned} \tag{A.1}$$

where  $\zeta = L\left(\frac{L\kappa+1}{\kappa+1}\right)$ .

The PDF of  $Y$  can be express as  $f_Y(y) = \frac{1}{\sigma_{re}^2} e^{-\frac{y}{\sigma_{re}^2}}$ , and  $X_r$ 's CDF and  $Z$ 's PDF denoted by (10) and (11), respectively. Combining (10), (11) and PDF of  $Y$ , (A.3) can be converted into integral form as

$$P_{out,r}^{ipSIC} = \int_0^\infty \int_0^D \frac{1}{\sigma_{re}^2} e^{-\frac{y}{\sigma_{re}^2}} \frac{2z}{D^2 \Gamma(p_r)} \gamma \left\{ p_r, \frac{1}{q_r} \sqrt{\frac{\hat{\gamma}_r d_s^\alpha}{a_r P_s^{act}} \left[ \zeta \frac{\sigma_s^2}{\eta_0^2} + \frac{z^\alpha}{\eta_0^2} \left( \frac{\varepsilon y P_s^{act}}{\beta_r \lambda} + \frac{\sigma_0^2}{\beta_r \lambda} \right) \right]} \right\} dz dy, \tag{A.4}$$

By applying Gauss-Chebyshev quadrature [56, Eq. (8.8.4)], the definite integral of above expression can be calculated as

$$P_{out,r}^{ipSIC} = \frac{\pi}{2U} \sum_{u=1}^U \int_0^\infty e^{-\frac{y}{\sigma_{re}^2}} \frac{(x_u+1)}{\sigma_{re}^2 \Gamma(p_r)} \sqrt{1-x_u^2} \gamma \left\{ p_r, \frac{1}{q_r} \sqrt{\frac{\hat{\gamma}_r d_s^\alpha}{a_r P_s^{act}} \left[ \zeta \frac{\sigma_s^2}{\eta_0^2} + \frac{\chi_u^\alpha}{\eta_0^2} \left( \frac{\varepsilon y P_s^{act}}{\beta_r \lambda} + \frac{\sigma_0^2}{\beta_r \lambda} \right) \right]} \right\} dy. \tag{A.5}$$

It can be seen that the above equation contains the term  $e^{-at}$  and the limits of integration are 0 to infinity. This type of integral equation can be calculated by applying Gauss-Laguerre quadrature formula [56, Eq. (8.6.5)], i.e.,  $\int_0^\infty e^{-at} f(t) dt = \frac{1}{a} \sum_{k=1}^K A_k f\left(\frac{x_k}{a}\right)$ . After some algebraic manipulations, we can obtain (14). The proof is complete.

## APPENDIX B: PROOF OF COROLLARY 3

To obtain the accurate asymptotic outage probability, the Laplace transform is applied in the following proof process. The Laplace transform formula of the PDF for  $X_\varphi^l$  is calculated by [51, Eq. (6.621.3)] as

$$\begin{aligned}
L \left[ f_{X_\varphi^l}(x) \right] (s) &= \sqrt{\pi} \sum_{u=0}^\infty \sum_{v=0}^\infty \frac{(1+\kappa)^{2(u+1)} 4^{u-v+1}}{\kappa^{-u-v} (u!)^2 (v!)^2 e^{2\kappa}} \frac{\Gamma(2+2u) \Gamma(2+2v)}{[s+2(\kappa+1)]^{2u+2} \Gamma(u+v+\frac{5}{2})} \\
&\times {}_2F_1 \left( 2+2u, \frac{1}{2}+u-v; \frac{5}{2}+u+v; \frac{-2(\kappa+1)+s}{2(\kappa+1)+s} \right).
\end{aligned} \tag{B.1}$$

When  $P_s^{act} \rightarrow \infty$ ,  $s$  in the above equation goes to infinity. At the same time, the first term ( $i = 0, j = 0$ ) of above series dominates the whole expression, thus the Laplace transform is eventually simplified as

$$\mathcal{L} \left[ f_{X_\varphi^l}(x) \right] (s) = {}_2F_1 \left( 2, \frac{1}{2}; \frac{5}{2}; 1 \right) \frac{16(1+\kappa)^2}{3e^{2\kappa}s^2}. \quad (\text{B.2})$$

As  $\sqrt{X_\varphi} = \sum_{l=1}^L |X_\varphi^l|$  and by applying the convolution theorem, the Laplace transform for the PDF of  $\sqrt{X_\varphi}$  can be given by

$$\mathcal{L} \left[ f_{\sqrt{X_\varphi}}^{0+}(x) \right] (s) = \left[ {}_2F_1 \left( 2, \frac{1}{2}; \frac{5}{2}; 1 \right) \frac{16(1+\kappa)^2}{3e^{2\kappa}} s^{-2} \right]^L. \quad (\text{B.3})$$

After using the inverse Laplace transform, the above expression can be derived as

$$f_{\sqrt{X_\varphi}}^{0+}(x) = \frac{x^{2L-1}}{(2L-1)!} \left[ {}_2F_1 \left( 2, \frac{1}{2}; \frac{5}{2}; 1 \right) \frac{16(1+\kappa)^2}{3e^{2\kappa}} \right]^L. \quad (\text{B.4})$$

Furthermore, by applying equation  $F_\chi(x) = \int_0^{\sqrt{x}} f_\chi(x) dx$ , the approximated CDF of  $X_\varphi$  at high SNRs can be finally expressed as

$$F_{X_\varphi}^{0+}(x) = \frac{\Lambda^L x^L}{(2L)!} \left[ {}_2F_1 \left( 2, \frac{1}{2}; \frac{5}{2}; 1 \right) \right]^L. \quad (\text{B.5})$$

Combining (B.5) and (A.3), (24) can be obtained after using Gauss-Laguerre quadrature and Gauss-Chebyshev quadrature. The proof is complete.

### APPENDIX C: PROOF OF THEOREM 3

The PDF and CDF of  $\gamma_r$  are first derived to facilitate the proof of the theorem. We note that the CDF of  $\gamma_r$  can be obtained by transforming (14) as

$$F_{\gamma_r}(x) = \sum_{k=1}^K \sum_{u=1}^U \frac{\pi(x_u+1) A_k}{2U\Gamma(p_r)} \sqrt{1-x_u^2} \gamma \left\{ p_r, \frac{\sqrt{x}}{q_r} \sqrt{\frac{d_s^\alpha}{a_r P_s^{act}} \left[ \zeta \frac{\sigma_s^2}{\eta_0} + \frac{\chi_u^\alpha}{\eta_0^2} \left( \frac{\varepsilon y_k P_s^{act}}{\beta_r \lambda \sigma_{re}^{-2}} + \frac{\sigma_0^2}{\beta_r \lambda} \right) \right]} \right\}, \quad (\text{C.1})$$

By taking the derivative of above equation, we can obtain the PDF expression for  $\gamma_r$  as

$$f_{\gamma_r}(x) = \pi \sum_{u=1}^U \sum_{k=1}^K \frac{\vartheta A_k (x_u+1) \sqrt{1-x_u^2}}{2U\Gamma(p_r) 2\sqrt{x} e^{\vartheta\sqrt{x}}} (\vartheta\sqrt{x})^{p_r-1}, \quad (\text{C.2})$$

where  $\vartheta = \frac{1}{q_r} \sqrt{\frac{d_s^\alpha}{a_r P_s^{act}} \left[ \zeta \frac{\sigma_s^2}{\eta_0} + \frac{\chi_u^\alpha}{\eta_0^2} \left( \frac{\varepsilon y_k P_s^{act}}{\beta_r \lambda \sigma_{re}^{-2}} + \frac{\sigma_0^2}{\beta_r \lambda} \right) \right]}$ .

By substituting (4) into (27), the ergodic data rate expression of  $U_r$  with ipSIC scheme is calculated as

$$R_{r,ipSIC}^{erg} = \left[ \log_2 \left( 1 + \frac{a_r \lambda \beta_r P_s^{act} |\mathbf{h}_s^H \mathbf{\Phi}_r \mathbf{h}_r|^2}{\lambda \beta_r |\mathbf{n}_s^H \mathbf{\Phi}_r \mathbf{h}_r|^2 + \varepsilon |h_{re}|^2 P_s^{act} + \sigma_0^2} \right) \right] = \frac{1}{\ln 2} \int_0^\infty \ln(1+x) f_{\gamma_r}(x) dx. \quad (\text{C.3})$$

By substituting (C.2) into (C.3), the expression of  $U_r$ 's ergodic data rate with ipSIC for ASTARS-NOMA networks can be given by

$$R_{r,ipSIC}^{erg} = \int_0^\infty \sum_{k=1}^K \sum_{u=1}^U \frac{\pi A_k(x_u+1) \ln(1+x^2) \sqrt{1-x_u^2}}{2U \ln 2 \Gamma(p_r) e^{\vartheta x} \vartheta^{-p_r} x^{1-p_r}} dx. \quad (C.4)$$

Also by using Gauss-Laguerre quadrature, (28) can be obtained. The proof is complete.

#### APPENDIX D: PROOF OF THEOREM 4

The expression for  $F_{\gamma_t}(x)$  can be obtained by transforming (18) as

$$F_{\gamma_t}(x) = \sum_{u=1}^U \gamma \left[ p_t, \sqrt{\frac{x d_s^\alpha q_t^{-2}}{P_s^{act} (a_t - x a_r)} \left( \frac{y_u^\alpha \sigma_0^2}{\eta_0^2 \beta_t \lambda} + \zeta \frac{\sigma_s^2}{\eta_0} \right)} \right] \frac{\pi(x_u+1)}{2U \Gamma(p_t)} \sqrt{1-x_u^2}. \quad (D.1)$$

Different from (C.1), the  $x$  in (D.1) needs to satisfy the inequality  $x < \frac{a_t}{a_r}$ . Thus the ergodic data rate expression of  $U_t$  is calculated as

$$R_t^{erg} = \frac{1}{\ln 2} \int_0^{\frac{a_t}{a_r}} f_{\gamma_t}(x) \ln(1+x) dx = \frac{1}{\ln 2} \int_0^{\frac{a_t}{a_r}} \frac{1}{1+x} [1 - F_{\gamma_t}(x)] dx. \quad (D.2)$$

By substituting (D.1) into (D.2), the expression of  $U_t$ 's ergodic data rate for ASTARS-NOMA networks is given by

$$R_t^{erg} = \frac{1}{\ln 2} \int_0^{\frac{a_t}{a_r}} \frac{1}{1+x} \left\{ 1 - \sum_{u=1}^U \frac{\pi(x_u+1)}{2U \Gamma(p_t)} \sqrt{1-x_u^2} \gamma \left[ p_t, \frac{1}{q_t} \sqrt{\frac{x d_r^\alpha}{(a_t - x a_r) P_s^{act}} \left( \frac{y_u^\alpha \sigma_0^2}{\eta_0^2 \beta_t \lambda} + \zeta \frac{\sigma_s^2}{\eta_0} \right)} \right] \right\} dx. \quad (D.3)$$

The definite integral in (D.3) can be calculated by applying Gauss-Chebyshev quadrature. After some simple mathematical calculations, we can figure out (30). The proof is complete.

#### REFERENCES

- [1] Z. Zhang, Y. Xiao, Z. Ma, M. Xiao, Z. Ding, X. Lei, G. K. Karagiannidis, and P. Fan, "6G wireless networks: Vision, requirements, architecture, and key technologies," *IEEE Veh. Technol. Mag.*, vol. 14, no. 3, pp. 28–41, Sept. 2019.
- [2] M. Giordani, M. Polese, M. Mezzavilla, S. Rangan, and M. Zorzi, "Toward 6G networks: Use cases and technologies," *IEEE Commun. Mag.*, vol. 58, no. 3, pp. 55–61, Mar. 2020.
- [3] E. Basar, M. Di Renzo, J. De Rosny, M. Debbah, M.-S. Alouini, and R. Zhang, "Wireless communications through reconfigurable intelligent surfaces," *IEEE Access*, vol. 7, pp. 116 753–116 773, Aug. 2019.
- [4] Q. Wu and R. Zhang, "Towards smart and reconfigurable environment: Intelligent reflecting surface aided wireless network," *IEEE Commun. Mag.*, vol. 58, no. 1, pp. 106–112, Jan. 2020.
- [5] L. Yang, J. Yang, W. Xie, M. O. Hasna, T. Tsiftsis, and M. D. Renzo, "Secrecy performance analysis of RIS-aided wireless communication systems," *IEEE Trans. Veh. Technol.*, vol. 69, no. 10, pp. 12 296–12 300, Oct. 2020.
- [6] K. Keykhosravi, M. F. Keskin, S. Dwivedi, G. Seco-Granados, and H. Wymeersch, "Semi-passive 3D positioning of multiple RIS-enabled users," *IEEE Trans. Veh. Technol.*, vol. 70, no. 10, pp. 11 073–11 077, Oct. 2021.

- [7] L. Yang, F. Meng, J. Zhang, M. O. Hasna, and M. D. Renzo, "On the performance of RIS-assisted dual-hop UAV communication systems," *IEEE Trans. Veh. Technol.*, vol. 69, no. 9, pp. 10385–10390, Sept. 2020.
- [8] Y. Liu, X. Liu, X. Mu, T. Hou, J. Xu, M. D. Renzo, and N. Al-Dhahir, "Reconfigurable intelligent surfaces: Principles and opportunities," *IEEE Commun. Surveys Tutorials*, vol. 23, no. 3, pp. 1546–1577, Thirdquarter 2021.
- [9] M. Zeng, X. Li, G. Li, W. Hao, and O. A. Dobre, "Sum rate maximization for IRS-assisted uplink NOMA," *IEEE Commun. Lett.*, vol. 25, no. 1, pp. 234–238, Jan. 2021.
- [10] H. Zhang, S. Zeng, B. Di, Y. Tan, M. D. Renzo, M. Debbah, Z. Han, H. V. Poor, and L. Song, "Intelligent omni-surfaces for full-dimensional wireless communications: Principles, technology, and implementation," *IEEE Commun. Mag.*, vol. 60, no. 2, pp. 39–45, Feb. 2022.
- [11] H. Zhang and B. Di, "Intelligent omni-surfaces: Simultaneous refraction and reflection for full-dimensional wireless communications," *IEEE Commun. Surveys Tutorials*, vol. 24, no. 4, pp. 1997–2028, Fourthquarter. 2022.
- [12] Y. Liu, X. Mu, J. Xu, R. Schober, Y. Hao, H. V. Poor, and L. Hanzo, "STAR: Simultaneous transmission and reflection for 360° coverage by intelligent surfaces," *IEEE Wireless Commun.*, vol. 28, no. 6, pp. 102–109, Dec. 2021.
- [13] X. Mu, Y. Liu, L. Guo, J. Lin, and R. Schober, "Simultaneously transmitting and reflecting (STAR) RIS aided wireless communications," *IEEE Trans. Wireless Commun.*, vol. 21, no. 5, pp. 3083–3098, May. 2022.
- [14] Y. Zhang, B. Di, H. Zhang, M. Dong, L. Yang, and L. Song, "Dual codebook design for intelligent omni-surface aided communications," *IEEE Trans. Wireless Commun.*, vol. 21, no. 11, pp. 9232–9245, Fourthquarter. 2022.
- [15] X. Zhai, G. Han, Y. Cai, Y. Liu, and L. Hanzo, "Simultaneously transmitting and reflecting (STAR) RIS assisted over-the-air computation systems," *IEEE Trans. Veh. Technol.*, vol. 71, no. 3, pp. 1309–1322, Mar. 2023.
- [16] J. Xu, Y. Liu, X. Mu, R. Schober, and H. V. Poor, "STAR-RISs: A correlated T&R phase-shift model and practical phase-shift configuration strategies," *IEEE Trans. Wireless Commun.*, vol. 16, no. 5, pp. 1097–1111, Aug. 2022.
- [17] Z. Zhang, Z. Wang, Y. Liu, B. He, L. Lv, and J. Chen, "Security enhancement for coupled phase-shift STAR-RIS networks," *IEEE Trans. Veh. Technol.*, Early Access, 2023.
- [18] W. U. Khan, J. Liu, F. Jameel, V. Sharma, R. Jantti, and Z. Han, "Spectral efficiency optimization for next generation NOMA-enabled IoT networks," *IEEE Trans. Veh. Technol.*, vol. 69, no. 12, pp. 15284–15297, Dec. 2020.
- [19] Y. Liu, S. Zhang, X. Mu, Z. Ding, R. Schober, N. Al-Dhahir, E. Hossain, and X. Shen, "Evolution of NOMA toward next generation multiple access (NGMA) for 6G," *IEEE J. Sel. Areas Commun.*, vol. 40, no. 4, pp. 1037–1071, Apr. 2022.
- [20] Y. Yuan, Y. Wu, Z. Ding, X. You, H. V. Poor, and L. Hanzo, "NOMA for next-generation massive IoT: Performance potential and technology directions," *IEEE Commun. Mag.*, vol. 59, no. 7, pp. 115–121, Jul. 2021.
- [21] Z. Ding, M. Peng, and H. V. Poor, "Cooperative non-orthogonal multiple access in 5G systems," vol. 19, no. 8, pp. 1462–1465, Aug. 2015.
- [22] X. Yue, Y. Liu, S. Kang, A. Nallanathan, and Z. Ding, "Exploiting full/half-duplex user relaying in NOMA systems," vol. 66, no. 2, pp. 560–575, Feb. 2018.
- [23] Z. Ding, R. Schober, and H. V. Poor, "On the impact of phase shifting designs on IRS-NOMA," vol. 9, no. 10, pp. 1596–1600, Oct. 2020.
- [24] F. Fang, Y. Xu, Q.-V. Pham, and Z. Ding, "Energy-efficient design of IRS-NOMA networks," *IEEE Trans. Veh. Technol.*, vol. 69, no. 11, pp. 14088–14092, Nov. 2020.
- [25] X. Yue and Y. Liu, "Performance analysis of intelligent reflecting surface assisted NOMA networks," vol. 21, no. 4, pp. 2623–2636, Apr. 2022.
- [26] J. Zuo, X. Mu, and Y. Liu, "Non-orthogonal multiple access for near-field communications," May. 2023. [Online]. Available: <https://arxiv.org/abs/2304.13185v2>

- [27] Z. Ding, R. Schober, and H. V. Poor, "NOMA-based coexistence of near-field and far-field massive MIMO communications," *IEEE Wireless Commun. Lett.*, Early Access, 2023.
- [28] S. M. R. Islam, N. Avazov, O. A. Dobre, and K. sup Kwak, "Power-domain non-orthogonal multiple access (NOMA) in 5G systems: Potentials and challenges," *IEEE Commun. Surveys Tutorials*, vol. 19, no. 2, pp. 721–742, Secondquarter. 2017.
- [29] M. Aldababsa, A. Khaleel, and E. Basar, "STAR-RIS-NOMA networks: An error performance perspective," *IEEE Commun. Lett.*, vol. 26, no. 8, pp. 1784–1788, Aug. 2022.
- [30] C. Zhang, W. Yi, Y. Liu, Z. Ding, and L. Song, "STAR-IOs aided NOMA networks: Channel model approximation and performance," *IEEE Trans. Wireless Commun.*, vol. 21, no. 9, pp. 6861–6876, Sept. 2022.
- [31] X. Yue, J. Xie, Y. Liu, R. Liu, Z. Han, and Z. Ding, "Simultaneously transmitting and reflecting reconfigurable intelligent surface assisted NOMA networks," *IEEE Trans. Wireless Commun.*, vol. 22, no. 1, pp. 189–204, Jan. 2023.
- [32] C. Wu, X. Mu, X. Gu, and O. A. Dobre, "Coverage characterization of STAR-RIS networks: NOMA and OMA," *IEEE Commun. Lett.*, vol. 25, no. 9, pp. 3036–3040, Sept. 2021.
- [33] X. Li, Y. Zheng, M. Zeng, Y. Liu, and O. A. Dobre, "Enhancing secrecy performance for STAR-RIS NOMA networks," *IEEE Trans. Veh. Technol.*, vol. 72, no. 2, pp. 2684–2688, Feb. 2023.
- [34] C. Wu, X. Mu, Y. Liu, X. Gu, and X. Wang, "Resource allocation in STAR-RIS-aided networks: OMA and NOMA," *IEEE Trans. Wireless Commun.*, vol. 21, no. 9, pp. 7653–7667, Sept. 2022.
- [35] W. Ni, Y. Liu, Y. C. Eldar, Z. Yang, and H. Tian, "STAR-RIS integrated no-northogonal multiple access and over-the-air federated learning: Framework, analysis, and optimization," *IEEE Internet Things J.*, vol. 9, no. 18, pp. 17 136–17 156, Sept. 2022.
- [36] Z. Zhang, L. Dai, X. Chen, C. Liu, F. Yang, R. Schober, and H. V. Poor, "Active RIS vs. passive RIS: Which will prevail in 6G?" *IEEE Trans. Commun.*, vol. 71, no. 3, pp. 1707–1725, Mar. 2023.
- [37] Y. P. R. Long, Y.-C. Liang and E. G. Larsson, "Active reconfigurable intelligent surface aided wireless communications," *IEEE Trans. Wireless Commun.*, vol. 20, no. 8, pp. 4962–4975, Aug. 2021.
- [38] E. Basar and H. V. Poor, "Present and future of reconfigurable intelligent surface-empowered communications," *IEEE Signal Process. Mag.*, vol. 38, no. 6, pp. 146–152, Nov. 2021.
- [39] K. Zhi, C. Pan, H. Ren, K. Chai, and M. ElKashlan, "Active RIS versus passive RIS: Which is superior with the same power budget?" *IEEE Commun. Lett.*, vol. 26, no. 5, pp. 1150–1154, May. 2022.
- [40] G. Chen, Q. Wu, C. He, W. Chen, J. Tang, and S. Jin, "Active IRS aided multiple access for energy-constrained IoT systems," *IEEE Trans. Wireless Commun.*, vol. 22, no. 3, pp. 1677–1694, Mar. 2023.
- [41] Y. Zhu, Y. Liu, M. Li, Q. Wu, and Q. Shi, "A flexible design for active reconfigurable intelligent surfacea sub-array architecture," *IEEE Trans. Veh. Technol.*, Early Access, 2023.
- [42] J. Xu, J. Zuo, J. T. Zhou, and Y. Liu, "Active simultaneously transmitting and reflecting (STAR)-RISs: Modelling and analysis," Feb. 2023. [Online]. Available: <https://arxiv.org/abs/2302.04432>
- [43] Y. Ma, M. Li, Y. Liu, Q. Wu, and Q. Liu, "Optimization for reflection and transmission dual-functional active RIS-assisted systems," Early Access, 2023.
- [44] Y. Guo, Y. Liu, Q. Wu, Q. Shi, and Y. Zhao, "Enhanced secure communication via novel double-faced active RIS," *IEEE Trans. Wireless Commun.*, vol. 71, no. 6, pp. 3497– 3512, Jun. 2023.
- [45] K. K. Kishor and S. V. Hum, "An amplifying reconfigurable reflectarray antenna," *IEEE Trans. Antennas Propag.*, vol. 60, no. 1, pp. 197–205, Jun. 2012.
- [46] J. Bousquet, S. Magierowski, and G. G. Messier, "A 4-GHz active scatterer in 130-nm CMOS for phase sweep amplify-and-forward," *IEEE Trans. Circuits Syst. I, Reg. Papers*, vol. 59, no. 3, pp. 529–540, Mar. 2012.

- [47] J. Loncar, Z. Sipus, and S. Hrbar, "Ultrathin active polarizationselective metasurface at X-band frequencies," *Physical Review B*, vol. 100, no. 7, p. 075131, Oct. 2019.
- [48] M. Jereminov, A. Pandey, D. M. Bromberg, X. Li, G. Hug, and L. Pileggi, "Steady-state analysis of power system harmonics using equivalent split-circuit models," *IEEE PES Innovative Smart Grid Tech. Conf. Europe (ISGT-Europe)*, pp. 1–6, Ljubljana, Slovenia, Otc. 2016.
- [49] M. K. Simon, *Probability Distributions Involving Gaussian Random Variables*. Springer US, 2006.
- [50] S. Primak, V. Kontorovich, and V. Lyandres, *Stochastic Methods and their Applications to Communications: Stochastic Differential Equations Approach*, West Sussex, U.K.: Wiley, 2004.
- [51] I. S. Gradshteyn and I. M. Ryzhik, *Table of Integrals, Series and Products*, 6th ed. New York, NY, USA: Academic Press, 2000.
- [52] J. Laneman, D. Tse, and G. Wornell, "Cooperative diversity in wireless networks: Efficient protocols and outage behavior," vol. 50, no. 12, pp. 3062–3080, Dec. 2004.
- [53] C. Zhong, H. A. Suraweera, G. Zheng, I. Krikidis, and Z. Zhang, "Wireless information and power transfer with full duplex relaying," *IEEE Trans. Commun.*, vol. 62, no. 10, pp. 3447–3461, Oct. 2014.
- [54] L. Zheng and D. N. C. Tse, "Diversity and multiplexing: A fundamental tradeoff in multiple-antenna channels," *IEEE Trans. Inf. Theory*, vol. 45, no. 5, pp. 1073– 1096, May. 2003.
- [55] J. Xu, Y. Liu, X. Mu, and O. A. Dobre, "STAR-RISs: Simultaneous transmitting and reflecting reconfigurable intelligent surfaces," *IEEE Commun. Lett.*, vol. 25, no. 9, pp. 3134–3138, Sept. 2022.
- [56] E. Hildebrand, *Introduction to numerical analysis*, New York, NY, USA: Dover, 1987.